

Multipoint Dixon Technique for Water and Fat Proton and Susceptibility Imaging¹

Gary H. Glover, PhD

Extensions to a previously described three-point Dixon magnetic resonance imaging technique are presented that use alternative water/fat phase-encoding strategies. The technique is generalized to phase encoding of $(-\theta, 0, \theta)$ or $(0, \theta, 2\theta)$ radians, and the signal-to-noise ratio (S/N) performance is evaluated. It was found that a θ of $2\pi/3$ radians has optimal S/N but that a θ of π radians is a good compromise and that phase encoding of $(0, \pi, 2\pi)$ radians offer an advantage over the previous method, which used $(-\pi, 0, \pi)$ increments, in that a T_2' (intravoxel susceptibility dephasing) image may be obtained in addition to the usual water, fat, and B_0 images. A new four-point method with phase encoding of $(0, \pi, 2\pi, 3\pi)$ radians that can also provide a measure of the spectral width of the fat resonance is suggested. The disadvantages of the method are the extra imaging time and low S/N efficiency.

Index terms: Chemical shift • Image processing • Phase-contrast imaging • Physics • Pulse sequences • Reconstruction algorithms

JMRI 1991; 1:521-530

Abbreviations: 4PD = four-point Dixon, NSA = number of signals averaged, RF = radio frequency, S/N = signal-to-noise ratio, 3PD = three-point Dixon, 2PD = two-point Dixon.

THE IN VIVO HUMAN PROTON SPECTRUM contains two dominant peaks, water and fat. In principle, therefore, chemical shift-resolved proton magnetic resonance (MR) imaging requires only two measurements per voxel if one assumes that (a) the magnetic field is homogeneous to a small fraction of the water/fat chemical shift, (b) the spectral width of each component is negligible, and (c) intravoxel amplitude losses due to phase dispersion and/or diffusion are negligible. Using such assumptions, Dixon developed a technique that employs two acquisitions. In the first, the phase difference between fat and water signals is adjusted to 0 radians, and in the second, the difference is adjusted to π radians (1). Addition and subtraction of the two acquired complex images results in separate water and fat images.

Errors in the use of two-point Dixon (2PD) techniques in which either the shim is poor or the chemical shift is incorrectly assumed have been reported previously (2). Others have discussed the quality of fat suppression obtained with 2PD methods when T_2^* differs for the two components, and a four-cycle sequence was proposed to diminish the attendant errors (3). Still other work has used multiple echoes to remove ambiguities in the unwrapping of phase in the presence of B_0 inhomogeneities (4).

The three conditions described above as simultaneously necessary for proper operation of the Dixon technique are rarely satisfied in practice. The first of these, field homogeneity, is often severely violated. Even if the magnetic field can be initially adjusted for perfect homogeneity, insertion of the subject into the magnet alters the field by establishing local perturbations that are of too short a spatial extent for shimming to be effective (5). Such perturbations cause failures of the Dixon method (6,7) and of other chemical shift selective methods (eg, fat suppression [3,8] or water selection [9]).

The second condition tacitly assumed in the Dixon method is that the spectrum consists of two δ functions that are separated by the chemical shift. In reality, the intrinsic linewidths are determined in the fast-motion limit by T_2 for the water component and by

¹ From the Department of Diagnostic Radiology and Nuclear Medicine, S-047, Stanford University School of Medicine, 300 Pasteur Dr., Stanford, CA 94305-5105. Received March 4, 1991; revision requested June 18; revision received and accepted July 9. Supported in part by GE Medical Systems. Address reprint requests to the author.

© SMRI, 1991

the several lipid resonances (10), which thereby complicate the fat peak.

The fat "peak" comprises several components, of which some are spin coupled and as such do not constitute a simple line of narrow width. Rather, the fat signal is found to be modulated by an oscillatory function of the J-coupling frequency, which therefore causes the spin-echo amplitude to depend on TE (11). A similar modulation caused by the multiple lines is observed on gradient-echo images as TE is varied (12). In the distal femur, for example, the yellow marrow contains exclusively fatty components, and diffraction between the olefinic and aliphatic fatty acid signals causes oscillatory behavior (13). In addition, the trabecular structure can cause all the lines to be broadened by susceptibility dephasing.

One approach toward characterizing the fat complex is to model the signal as a T_2^* -weighted series of sine waves and fit the model with data obtained by means of gradient-echo interferometry (13). This method requires many acquisitions, with TE varied to obtain sufficient data for the model fitting to converge, and therefore is not necessarily time efficient. Moreover, the results depend sensitively on noise and the starting conditions of the χ^2 minimization procedure; the method is therefore not robust. The model used a common T_2^* loss factor for the water and fat components because the susceptibility dephasing loss dominated the fat line broadening. This assumption is not valid in other structures (eg, subcutaneous fat or liver).

The third assumption made in Dixon techniques is that amplitude losses in the opposed-phase measurement can be ignored. Such losses can arise, however, from intravoxel phase dispersion caused by microscopic susceptibility variations in the lung (14) or in trabecular bone (12,15), as well as near the orbits or air passages. In other cases, diffusion losses may be significant (16).

The first difficulty, that of magnetic field heterogeneity, has been addressed recently with the use of a three-point Dixon (3PD) method (6,17), although many other approaches have been demonstrated (eg, [4]). This 3PD technique augments the two measurements of the original Dixon technique with a third measurement that has a water/fat chemical shift phase encoding of $-\pi$ radians. This allows calculation of the B_0 field in each voxel and provides a mathematical method of locally "shimming" each voxel with retrospective correction of the data. This in turn enables perfect separation of water and fat components and supplies a B_0 image that is indicative of macroscopic susceptibility variations. This technique has proved more robust than fat saturation methods and has found application in prostate imaging (7), in which reliable suppression of the fat signal allows reduction of the acquisition bandwidth for increased signal-to-noise ratio (S/N) without incurring chemical shift artifacts. The fat image has also proved useful in the assessment of extracapsular invasion by tumor.

Although the 3PD method has been highly successful, two aspects can be improved. The first is that the B_0 calculation can be indeterminate for voxels containing an admixture of water and fat because of signal cancellation on the two out-of-phase ($\pm\pi$) images

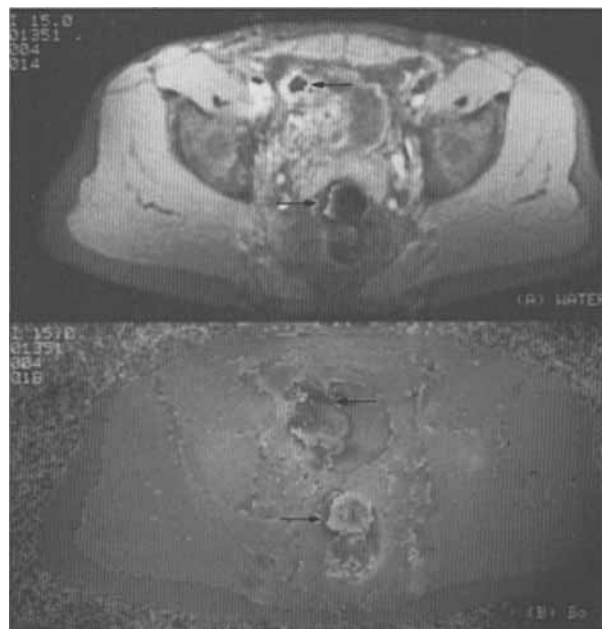


Figure 1. Three-point Dixon images (water, upper; B_0 , lower) obtained with the previous method ($-\pi, 0, \pi$) (17) show artifacts (arrows) at tissue-air interfaces and at partial-volume boundaries where water and fat signals cancel.

used to measure B_0 . An example of this effect is shown in Figure 1, in which voxels that span transitions between water and fat have indeterminate phase due to signal dropout. Note, however, that the fat/water separation is not jeopardized by the ambiguity.

The second, and more important, shortcoming of the 3PD technique is that no correction is made for intravoxel amplitude loss on the $\pm\pi$ images. This effect is normally negligible but may be important, for example, in imaging trabecular bone (13). In such cases, there may be diagnostic utility in providing a map of amplitude loss due to dephasing, in addition to correcting the water/fat decomposition. Moreover, it may also be desirable to attempt to more fully account for the complexity of the fat resonance, which can also cause signal loss from dispersive addition of its several components.

Thus, it is useful to examine alternatives to the present 3PD method to attempt to surmount the above limitations and to extend the utility of such chemical shift-resolved imaging methods. To this end, a general formulation of three-point methods defined with water/fat phase-encoding values of $(-\theta, 0, \theta)$ or $(0, \theta, 2\theta)$ radians is presented in this report, and the S/N performance is calculated. In addition, the method has been extended to include a fourth measurement point. Two practical extensions of the method have emerged.

The first extension involves altering the chemical shift phase encoding to increments of $(0, \pi, 2\pi)$ radians to eliminate transition-voxel signal dropout in the B_0 calculation and to provide a map of T_2' (the field heterogeneity loss component of T_2^*) in cases in which the spectral complexity of fat may be ignored.

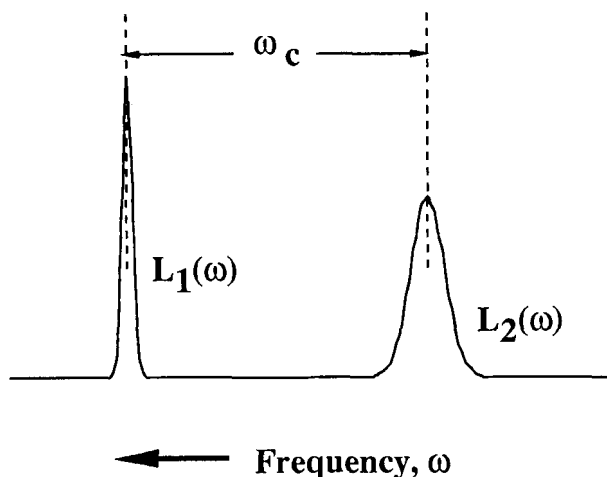


Figure 2. Proton chemical shift spectrum modeled as two components, $L_1(\omega)$ and $L_2(\omega)$. ω_c = chemical shift.

This technique requires no additional imaging time beyond that of the original method.

In the application of this modified 3PD method, one finds that the resulting T2' images show spuriously shortened values in subcutaneous fat. This is caused by breakdown of the assumption that the fat signal is a single line with the same spectral width as that of water. A more complete model retains the fat complex as a single line but allows its width to differ from that of water. Although this model is highly simplified, it affords adequate flexibility for characterizing fat signals, as will be shown.

The second extension of the original method uses four measurements with water/fat phase encodings of $(0, \pi, 2\pi, 3\pi)$ radians. While this method requires additional imaging time, it provides the added degree of freedom necessary to describe one additional component of the fat complex. Because we have chosen here to model the fat as a single broad peak, its linewidth may be determined subject to the limitations of this model. This may be important in quantitation of bone marrow.

It is noted in passing that the Dixon technique was also extended to more points by Sepponen et al (18), but this was done to increase chemical shift resolution rather than correct for other errors, as in the two-species techniques presently under discussion.

The following section presents a generalized theory for these methods. The traditional 2PD and previous 3PD methods are found to be special cases of the more general formulation.

• THEORY AND METHODS

General Considerations

Consider a model in which there are two chemical shift components (water and fat) with a spectrum $L(\omega)$ that may be decomposed into two components $L_1(\omega)$ (water) and $L_2(\omega)$ (fat), as shown in Figure 2. Let ρ_1 and ρ_2 , respectively, be the integrated real-value intensities of these lines in a nuclear MR experiment. These quantities are therefore weighted by T1 and T2

according to the TR and TE used. The chemical shift is ω_c , as shown.

Suppose now that multipoint Dixon acquisitions are performed with either pulse sequence shown in Figure 3. N acquisitions are performed with a τ increment between samples according to

$$\omega_c \tau_n = \theta_n, \quad (1)$$

where n spans the N measurements. In the case of the gradient-recalled-echo sequence (Fig 3b), it is assumed that TE is much less than T2, so that differences in T2 losses between acquisitions may be ignored. In such a case, or in the spin-echo case, voxel intensities for the complex images obtained for each τ_n are

$$S_n = [\rho_1 A_1(\tau_n) + \rho_2 A_2(\tau_n) e^{i\theta_n}] e^{i(\omega_0 \tau_n + \phi_0)}, \quad (2)$$

where A_1 and A_2 represent amplitude loss factors for water and fat, respectively, which depend on τ and could be different for the two species; ϕ_0 is a phase shift independent of acquisition number n (but which may be voxel dependent); and ω_0 is the resonance offset of the water (ρ_1) line. ϕ_0 arises, for example, from systemic phase shifts in the RF system (coil, transmitter, and receiver) or from RF penetration effects due to standing waves and dielectric losses in the subject. ω_0 allows for voxel-dependent B_0 shifts due to shim heterogeneity or susceptibility.

Let us now examine the physical basis for the amplitude loss factors A_1 and A_2 . Three possibilities can be postulated:

Diffusion.—In some tissue structures, susceptibility variations on a spatial scale that is small relative to an imaging resolution element (voxel) may establish fixed gradients G_s in the magnetic field that can attain substantial amplitudes. In this case, diffusion of the water molecules through the strong, self-induced gradient fields may result in diminution of the water signal (19). There is little self-diffusion of fat components, so that A_2 may be assumed to be unity (Le Bihan D, personal communication, 1991). For spin-echo acquisitions (20), A_1 due to diffusion of water molecules is

$$A_{1d}(\tau_n) = e^{-\gamma^2 G_s^2 D (\text{TE})^3 / 12 + (\tau_n / 2 \text{TE})^2} \quad (3)$$

where γ is the gyromagnetic ratio, D is the diffusion coefficient, and TE and τ_n are as indicated in Figure 3. For gradient-recalled sequences (Fig 3b),

$$A_{1d}(\tau_n) = e^{-\gamma^2 G_s^2 D (\text{TE} + \tau_n)^3 / 3}. \quad (4)$$

If τ_n is much less than TE, the diffusion loss terms (Eq [3], [4]) have only weak dependence on τ_n . In any case, diffusion effects are likely to be rather slight for most tissue structures (G_s small) and we may therefore approximate the water diffusion loss term A_{1d} as a constant and set the fat loss term to unity ($A_{2d} = 1$).

Susceptibility dephasing.—As in the diffusion mechanism, stationary gradients can be set up by susceptibility variations in the tissue microstructure. If these gradients have sufficiently short range, they may cause signal cancellation within a voxel (intra-voxel dephasing) because of the multiplicity of Larmor frequencies present in the voxel. This mechanism acts

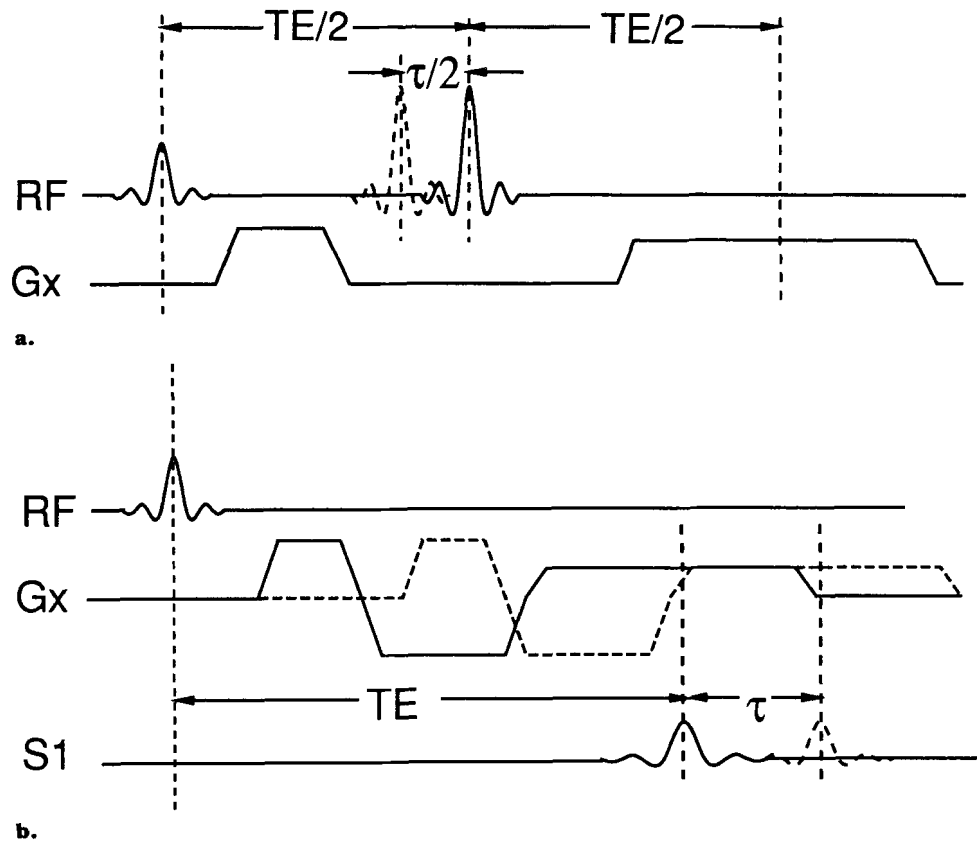


Figure 3. Simplified spin-echo (a) and gradient-recalled (b) pulse sequences for multipoint Dixon methods. Only two resonance-offset phase-encoding positions are shown. RF = radio frequency, S₁ = signal amplitude.

jointly on the two components of the admixture, so that

$$A_{1s} = A_{2s} \equiv A_s(\tau_n) = \int_{-\infty}^{\infty} \chi(\omega) e^{i\omega\tau_n} d\omega / \int_{-\infty}^{\infty} \chi(\omega) d\omega, \quad (5)$$

where $\chi(\omega)$ is the spectral distribution within a voxel. This may be written

$$A_s(\tau_n) = \hat{\chi}(\tau_n) / \hat{\chi}(0), \quad (6)$$

where $\hat{\chi} = \mathbf{F}(\chi)$, in which \mathbf{F} denotes the Fourier transform.

Assume for illustration a Lorentzian distribution; then,

$$A_s(\tau_n) = e^{-|\tau_n|/T_2'}, \quad (7)$$

where $1/T_2'$ is the characteristic half-width of the line.

Thus, susceptibility dephasing gives rise to a loss factor that is common to both chemical shift species but that depends on τ_n . In the special case of a Lorentzian distribution, this loss may be formulated in terms of a susceptibility dephasing time T_2' , which represents the field heterogeneity loss component of T_2^* :

$$1/T_2^* = 1/T_2 + 1/T_2'. \quad (8)$$

Although the monoexponential assignment of loss (Eq [7]) is not essential, it is convenient, for it allows one to use T_2' as a measure of coherence time and establishes a relationship with T_2^* through Equation (8).

Spectral broadening.—If the two components of the spectrum have finite intrinsic linewidths, loss of coherence will again occur by a phasor summation mechanism similar to that of Equation (5). Thus,

$$A_{kw}(\tau_n) = \int_{-\infty}^{\infty} L_k(\omega) e^{i\omega\tau_n} d\omega / \int_{-\infty}^{\infty} L_k(\omega) d\omega. \quad (9)$$

It has been found experimentally that in in vivo imaging of human subjects, voxels containing primarily water show little signal loss due to spectral broadening, while voxels containing primarily fat have observable loss. One may infer, therefore, that the water peak has a sharp line and $L_1(\omega) \approx \delta(\omega)$, so that $A_{1w} = 1$. The fat line, however, contains several components, and it is not unreasonable to allow its spectrum to be broadened. For a Gaussian fat line with half-width $\Delta\omega$,

$$A_{2w}(\tau_n) = e^{-(\Delta\omega\tau_n)^2/4}. \quad (10)$$

In general, all loss mechanisms could be operating. In that case, the total loss is obtained by multiplying all terms together:

$$A_k = A_{kd} \cdot A_{ks} \cdot A_{kw}, \quad (11)$$

where $k = 1, 2$.

Equation (2) cannot be solved without specification of the loss mechanisms and phase-encoding strategy. In previous work, attenuation loss was ignored. It is

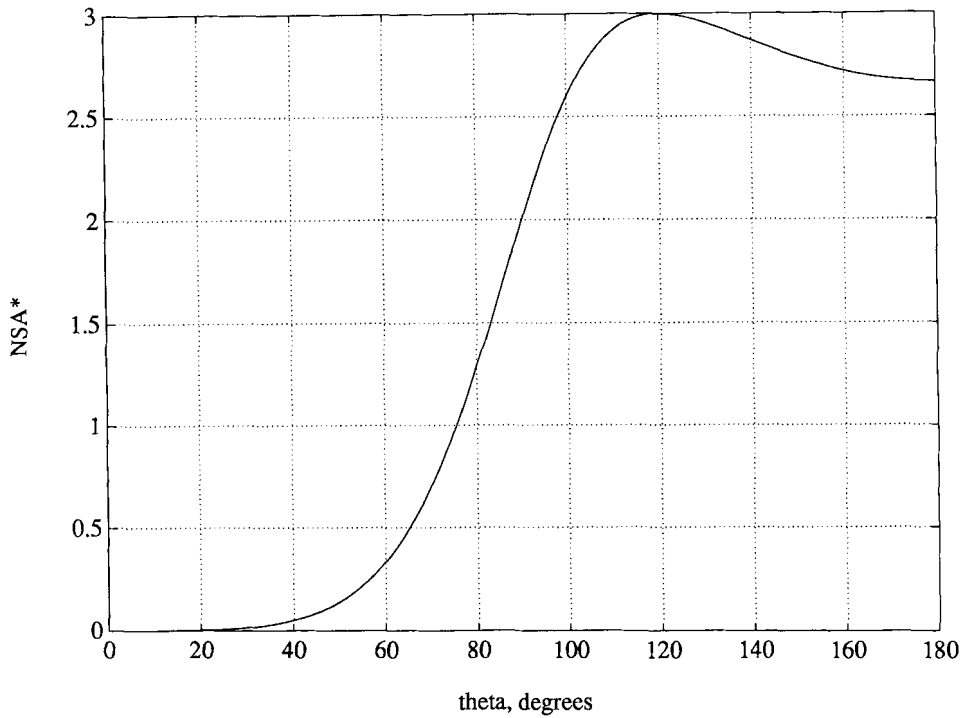


Figure 4. S/N efficiency (NSA*) versus resonance-offset phase-encoding increment θ .

instructive to examine these methods before extensions are considered.

2PD method.—The traditional 2PD method assumes $A_1 = A_2 = 1$, $\theta_1 = 0$, $\theta_2 = \pi$, and $\omega_0 = 0$. Then Equation (2) becomes

$$\left. \begin{aligned} S_0 &= (\rho_1 + \rho_2)e^{i\phi_0} \\ S_1 &= (\rho_1 - \rho_2)e^{i\phi_0} \end{aligned} \right\}, \quad (12)$$

for which separation into (real) water and fat images ρ_i is straightforward. With off resonance, however, the decomposition is not correct, and each image is an admixture of the two species. The 3PD method was developed to correct for this condition.

Symmetric 3PD method.—For the 3PD method previously described (17), $A_1 = A_2 = 1$, $\theta_{-1} = -\pi$, $\theta_0 = 0$, $\theta_1 = \pi$, and $\omega_0 \neq 0$ is allowed. We generalize here to symmetric phase encodings with $(-\theta, 0, \theta)$. Then,

$$\left. \begin{aligned} S_{-1} &= (\rho_1 + \rho_2 e^{-i\theta})e^{-i(\phi - \phi_0)} \\ S_0 &= (\rho_1 + \rho_2)e^{i\phi_0} \\ S_1 &= (\rho_1 + \rho_2 e^{i\theta})e^{i(\phi + \phi_0)} \end{aligned} \right\}, \quad (13)$$

where

$$\phi \equiv \omega_0 \tau_1. \quad (14)$$

The solution to Equations (13) is given by

$$\rho_{1,2} = S'_0/2 \pm 1/2 \sqrt{S'^2_0 - 2(S'_0{}^2 - S'_1 S'_{-1})/(1 - \cos \theta)}, \quad (15)$$

where

$$S'_n = S_n e^{-i\phi_0}. \quad (16)$$

The noise performance is described by the variance

of ρ_1 , which may be calculated assuming no cross correlation in the three acquired images. If the variance of these data is σ_0^2 , we have

$$\frac{\sigma_{\rho_1}^2}{\sigma_0^2} = \frac{1 + 2 \cos^2 \theta}{2(1 - \cos \theta)^2}. \quad (17)$$

This may also be expressed in terms of an S/N-equivalent number of signals averaged (NSA*) as

$$\sigma_{\rho_1} \equiv \frac{\sigma_0}{\sqrt{\text{NSA}^*}}, \quad (18)$$

where

$$\text{NSA}^* = \frac{2(1 - \cos \theta)^2}{1 + 2 \cos^2 \theta}. \quad (19)$$

Thus, NSA* denotes the NSA that is effective in noise reduction. For a three-point method, the best that can be done is an NSA* of 3.0. A plot of NSA* versus θ is shown in Figure 4. The pattern is mirror replicated beyond 180°. As can be seen, the maximum S/N is attained at a θ of 120°, where NSA* is the full 3.0. The previous 3PD method used a θ of 180°, for which NSA* is 2.67. These results indicate that the noise becomes very high as θ approaches zero, as would be expected, since the measurements become redundant. The optimum at 120° corresponds, not surprisingly, to a uniform spacing of phase encoding around the full 360° circle.

Addition of the extra measurement has provided the ability to calculate and correct for the resonance offset at little or no cost in S/N. Attenuation losses are not accounted for, however, and it is desirable to ex-

tend the 3PD method to address this need. Several levels of complexity may be considered, depending on the importance of each of the loss mechanisms described above. Two cases will be examined here; they lead to an extended 3PD method and a new four-point Dixon (4PD) method.

Extended 3PD Method

As a first extension to the method above, let us assume that diffusion losses are negligible and that spectral broadening in the fat may be ignored as well. Then, only a common loss factor occurs, which depends on τ_n according to Equation (7). It remains to choose reasonable strategies for the phase-encoding values θ_n . Examination of Equations (2) and (7) shows that with symmetric θ_n , the S_1 and S_{-1} measurements are redundant for the determination of A . Therefore, it is necessary to choose an asymmetric sampling, and we use $(0, \theta, 2\theta)$ phase encoding. Then, from Equation (7), Equation (2) becomes

$$S_n = (\rho_1 + \rho_2 e^{in\theta}) A^n e^{i(n\phi + \phi_0)}, \quad (20)$$

where $n = 0, 1, 2$.

The solution of Equation (20) is not straightforward for general θ . A special case of great interest is $\theta = \pi$. In this case, Equation (20) becomes

$$\left. \begin{aligned} S_0 &= (\rho_1 + \rho_2) e^{i\phi_0} \\ S_1 &= (\rho_1 - \rho_2) A e^{i(\phi + \phi_0)} \\ S_2 &= (\rho_1 + \rho_2) A^2 e^{i(2\phi + \phi_0)} \end{aligned} \right\} \quad (21)$$

Because of the special choice of θ , and since ρ_i are real, the magnitude ratio of S_2 and S_0 allows the determination of A . With A known, the solution to Equations (21) is similar to that given in Equation (15). As before, ϕ_0 is obtained from $\arg(S_0)$. Then, with use of Equation (16), we have

$$\rho_1 + \rho_2 = S_0' = |S_0|, \quad (22)$$

$$(\rho_1 + \rho_2) A e^{i\phi} = S_1', \quad (23)$$

$$(\rho_1 + \rho_2) A^2 e^{i2\phi} = S_2'. \quad (24)$$

From Equations (22) and (24), ϕ and A are obtained as

$$2\phi = \arg(S_2') - \arg(S_0') \quad (25)$$

and

$$A^2 = |S_2|/|S_0|, \quad (26)$$

respectively. As before (17), care must be taken in unwrapping the phase with Equation (25) to avoid additive 2π ambiguities in the arctangents. This part of the algorithm is unchanged from that of the previous method. With A and ϕ known, ρ_i are obtained from Equations (22)–(24).

Because of S/N considerations, however, some care must be used in the correction for dephasing signal loss. For voxels with $A \approx 1$, Equations (22) and (24) may be added; then,

$$\left. \begin{aligned} \rho_1 + \rho_2 &= (|S_0| + |S_2|)/2 \\ \rho_1 - \rho_2 &= S_1' e^{-i\phi} \end{aligned} \right\} \quad (27)$$

from which ρ_i are easily obtained. The S/N performance for such voxels is identical to that of the earlier method ($\text{NSA}^* = 2.67$). For voxels in which $A < 1$ cannot be ignored, the decomposition is

$$\left. \begin{aligned} \rho_1 + \rho_2 &= |S_0| \\ \rho_1 - \rho_2 &= S_1' e^{-i\phi}/A \end{aligned} \right\} \quad (28)$$

In this case, S/N is at best equivalent to an NSA of 2 but depends on A .

Because of the S/N advantage of using Equation (27), it is prudent to examine the effect of using these equations even though $A \neq 1$. It is found that only a small error in ρ_i results when the loss is small. Let $A = 1 - \epsilon$, where ϵ is much less than 1. Then, with use of Equations (27) to calculate ρ_i , to first order,

$$\begin{aligned} \rho_{1,2}(\text{calc}) &\approx \frac{\rho_1 + \rho_2}{2} (1 - \epsilon) \pm \frac{\rho_1 - \rho_2}{2} (1 - \epsilon) \\ &= \rho_{1,2} (1 - \epsilon) = \rho_{1,2} A. \end{aligned} \quad (29)$$

Thus, the only error in ignoring A in the decomposition, to first order, is to introduce a multiplicative error in both ρ_1 and ρ_2 . This is not a serious error, and it can usually be ignored. Therefore, in the results presented here, Equations (27) were used for all voxels because of the superior S/N performance.

If A is ignored, it can be shown that Equation (19) applies in this new 3PD method as well. Thus, the use of θ equal to π yields an NSA^* of less than the maximum, 3.0. However, this choice is a good trade-off because it enables a greatly simplified calculation of A .

Thus, in the new 3PD method, S/N performance and imaging time are equivalent to those of the previous formulation, but an intravoxel dephasing amplitude image (A) or a T_2' image can be obtained (with use of Equation [7]) as well as the ρ_i and B_0 images.

4PD Method

Let us now relax the assumption that the water and fat lines of the proton spectrum must be infinitesimally narrow. As in the preceding discussion, it is assumed that only the fat resonance is sufficiently broadened to affect the decomposition. The additional degree of freedom requires inclusion of another measurement to allow evaluation of the effect of a finite linewidth. Only equal increments in phase encoding $(0, \theta, 2\theta, 3\theta)$ are considered here. Then, in accordance with the assumptions in Equation (9) and retaining susceptibility dephasing according to Equation (7), one may express Equation (2) as

$$S_n = (\rho_1 + \rho_2 e^{in\theta} W^n) A^n e^{i(n\phi + \phi_0)}, \quad (30)$$

where W is the loss factor resulting from the finite width of the fat spectrum. By equating A_1 and A , and A_2 and AW , Equation (30) may be written equivalently as

$$S_n = (\rho_1 A_1 + \rho_2 e^{in\theta} A_2) e^{i(n\phi + \phi_0)}. \quad (31)$$

A general solution of Equation (31) is difficult. However, examination suggests that the solution is substantially simplified (as in 3PD) if θ is equal to π . From an S/N point of view, this will not be the opti-

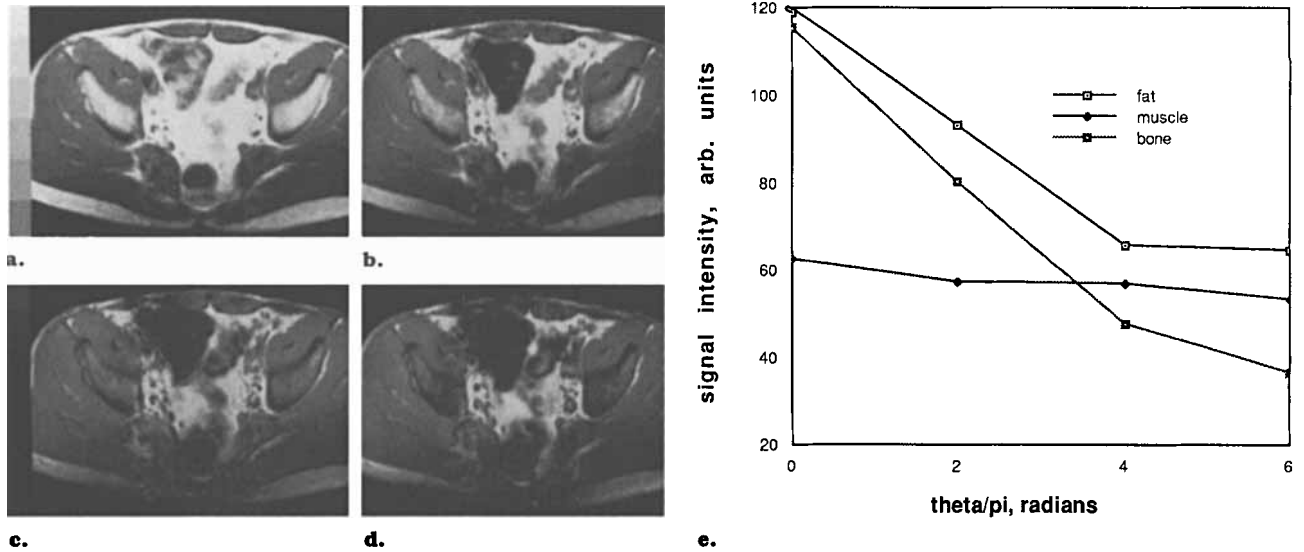


Figure 5. (a–d) Images with phase encoding of 0 (a), 2π (b), 4π (c), and 6π (d). (e) Plots of signal intensities in representative regions of interest. Signal loss in muscle and subcutaneous fat is small, whereas degradation in trabecular bone is substantial because of dephasing.

mum. In fact, we would expect the optimum to occur ($\text{NSA}^* = 4$) at a θ of $\pi/2$, which corresponds to an equal phasor spacing of the four acquisitions. With θ equal to π and with use of Equation (16),

$$\left. \begin{aligned} \rho_1 + \rho_2 &= S'_0 \\ \rho_1 A_1 - \rho_2 A_2 &= S'_1 e^{-i\phi} \\ \rho_1 A_1^2 + \rho_2 A_2^2 &= S'_2 e^{-i2\phi} \\ \rho_1 A_1^3 - \rho_2 A_2^3 &= S'_3 e^{-i3\phi} \end{aligned} \right\} \quad (32)$$

As before, 2ϕ may be obtained from $\arg(S'_2)$; then the right-hand side of Equations (32) is known.

To render these equations tractable, let us assume now that the amplitude losses are relatively small. Accordingly, let

$$A_k = 1 - \epsilon_k, \quad (33)$$

where ϵ_k is much less than 1. Keeping only first-order terms in ϵ , one obtains

$$\rho_1 = S'_0/2 + (3S'_1 - S'_3)/4, \quad (34)$$

$$\rho_2 = S'_0/2 - (3S'_1 - S'_3)/4, \quad (35)$$

$$A_1 = [S'_1 + (S'_2 + S'_0)/2]/2\rho_1, \quad (36)$$

$$A_2 = (\rho_1 A_1 - S'_1)/\rho_2 \quad (37)$$

where

$$S''_n \equiv S_n e^{-i(n\phi + \phi_0)}. \quad (38)$$

Thus, if the susceptibility and fat spectral impurity losses are not too severe, the 4PD method provides a means of determining the fat and water signal intensities, as well as resonance offsets and the spectral broadening and susceptibility loss components.

As shown with the 3PD method (Eq [19]), the S/N performance depends on the choice of phase increment. For the π increment used here, NSA^* is less than 4.0. From Equation (34), if the measurements

are independent and all have variance σ_0^2 ,

$$\left. \begin{aligned} \sigma_{\rho_1}^2 &= 7\sigma_0^2/8 \\ \sigma_{A_1}^2 &= \sigma_0^2/4 \end{aligned} \right\}, \quad (39)$$

which implies that the S/N equivalency for ρ_1 is an NSA^* of only $8/7$, despite spending 4.0 NSA of imaging time, although the determination of A_1 has a full 4.0 NSA S/N. Thus, a severe penalty has been exacted for choosing the phase-encoding steps (0, π , 2π , 3π) to simplify the analysis. Perhaps a more fair comparison with 2PD or the older 3PD methods is obtained by calculating the S/N in $\rho_1 A_1$, since that is the relevant function obtained with those techniques. From Equation (36), one obtains

$$\sigma_{\rho_1 A_1}^2 = \sigma_0^2/2, \quad (40)$$

so that the NSA^* for the case with loss is 2.

• RESULTS

The pulse sequences shown in Figure 3 and the new 3PD and 4PD reconstruction algorithms have been implemented on a 1.5-T imager (Signa; GE Medical Systems, Milwaukee). Figure 5a–5d shows in-phase magnitude images obtained at 0, 2π , 4π , and 6π radians, which therefore have different τ values but no fat-water signal cancellation. In Figure 5e signal intensity from these images for several tissue types is plotted as a function of the dephasing time τ . Note that there is little signal loss in muscle, in which no fat is present, but that there is loss in fat and substantial loss in bone. In accordance with the preceding discussion, an exponential dependence on τ is expected for either susceptibility loss or spectral broadening. The results are in qualitative agreement, suggesting that signal loss due to both susceptibility dephasing and fat complexity occurs in bone marrow, while only the fat line broadening occurs in subcutaneous tissue.

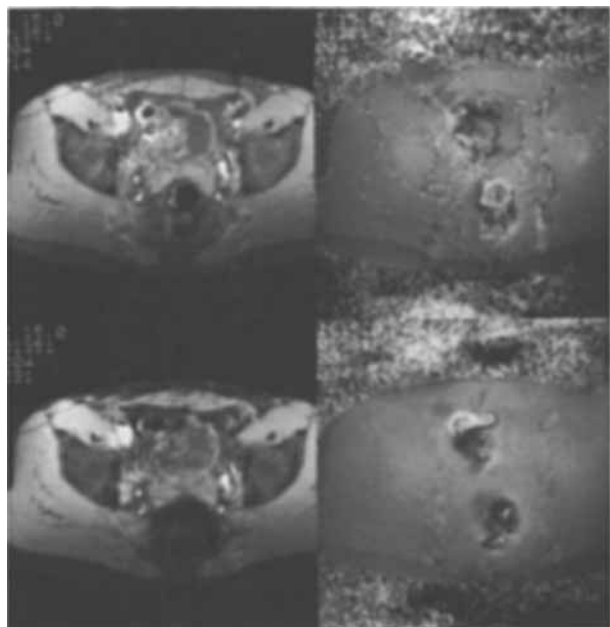


Figure 6. Comparison of old $(-\pi, 0, \pi)$ 3PD water image and B_0 map (top) versus new $(0, \pi, 2\pi)$ 3PD water image and B_0 map (bottom). Note the artifact-free B_0 map for the latter.

In Figure 6, the old $(-\pi, 0, \pi)$ and new $(0, \pi, 2\pi)$ 3PD methods are compared. The lower-right B_0 image in Figure 6 has no ambiguities at the water-fat boundaries as in the upper-right image. As a result, the water image (Fig 6, lower left) is accordingly free of isolated artifacts found with the original method (Fig 6, upper left). Figure 7 shows the full set of images obtained for one section imaged with the new 3PD method. In addition to water, fat, and B_0 images, a spin-echo image, an amplitude ratio (A) image, and a T_2' image are obtained. The A and T_2' images show increased susceptibility dephasing in trabecular bone. Note, however, that subcutaneous fat also shows apparent susceptibility loss. This can be related to a spectral broadening (W) of 0.85 in the region shown, which corresponds (from Eq [10]) to a Gaussian linewidth of 58 Hz, or 0.9 ppm.

Figure 8 shows an application of the 4PD method. Note here that the amplitude ratio image A_1 does not show apparent susceptibility loss in the fat as on the 3PD image. The amplitude loss in the fat signal due to broadening is observed on the A_2 image. Figure 9 is a comparison of the 3PD and 4PD methods. The water and fat images are similar in areas in which there is no overlap between species, but there are differences in trabecular bone regions, presumably due to the more accurate accounting for the finite fat linewidth with the 4PD method.

DISCUSSION

The new 3PD method eliminates artifacts seen with the previous technique, which resulted from signal cancellation in voxels containing admixtures of water and fat. The new method also provides an image of the amplitude loss occurring during the evolution time 2τ . In tissues containing primarily water, this

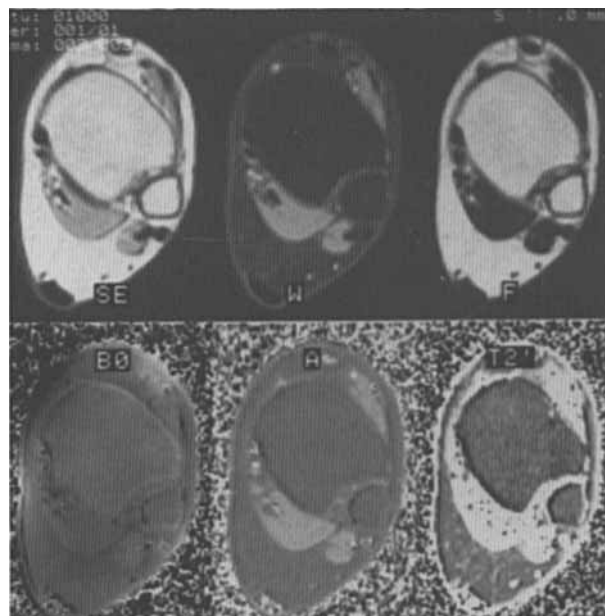


Figure 7. Complete set of 3PD images of leg: spin echo (SE), water (W), fat (F), B_0 , amplitude ratio (A), and T_2' . Amplitude dephasing image (A) shows reduction in signal intensity in subcutaneous fat because of finite linewidth.

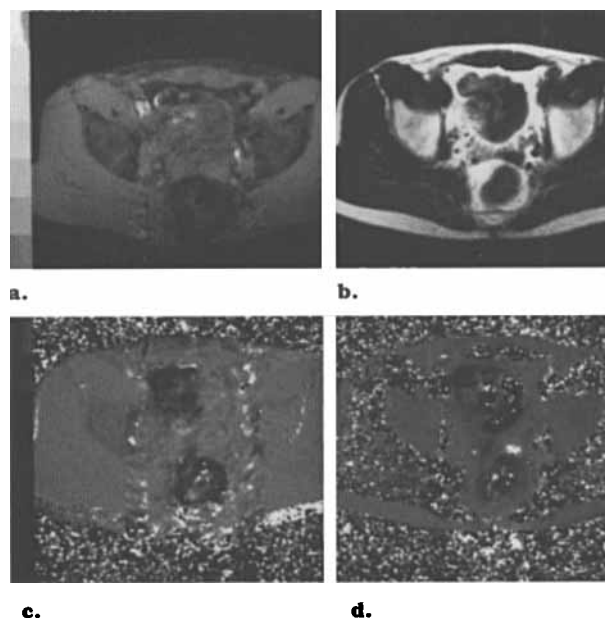


Figure 8. Water (a), fat (b), A_1 (c), and A_2 (d) images obtained with 4PD method. The A_2 image shows only fat and is indicative of linewidth of fat.

loss can be related to a susceptibility dephasing mechanism, while in fat the loss can be explained by spectral broadening in conjunction with dephasing. When the tissue contains both species, as in some forms of bone marrow, it is important to differentiate these two loss mechanisms. Unfortunately, this cannot be done with the 3PD method.

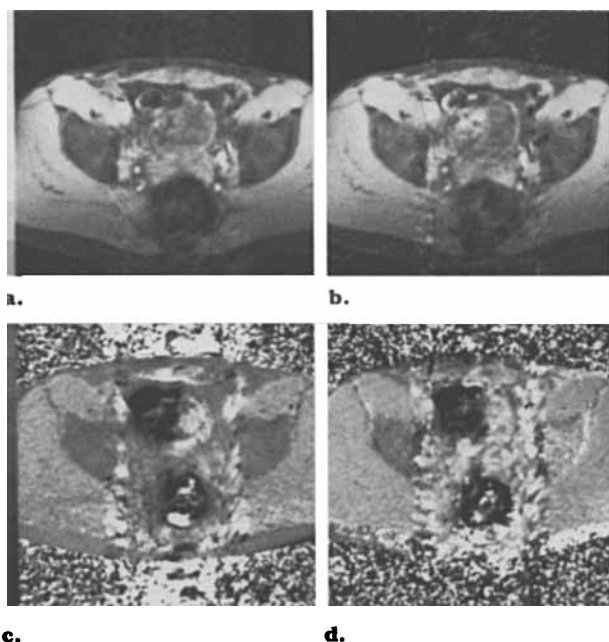


Figure 9. Comparison between 3PD (**a, c**) and 4PD (**b, d**) methods for water images (**a, b**) and A_1 images (**c, d**). Results are similar except in bone marrow, where the linewidth of fat alters the amplitude maps. The 4PD water image (**b**) is noisier, while the A_1 image (**d**) has a higher S/N, as expected.

The 4PD technique, however, can distinguish the two mechanisms, subject to the assumption that spectral broadening occurs only in the fat component. This provides more accurate decomposition of the water and fat image data. The price paid, of course, is that the imaging time must be increased to 4 NSA. Moreover, from Equation (39), the S/N for the water and fat images is equivalent to only 1.14 NSA, which reflects the high cost of the extra chemical shift resolution. In contrast, the 3PD method retains an S/N equivalence of 2.67 NSA. However, the A_1 and A_2 images have perfect (4 NSA) S/N performance with this choice of phase increment.

Of course, the model chosen here for the fat complex is obviously simplified in an attempt to allow characterization with just one additional parameter. Clearly this model may not be justified in some applications; in such cases, the T_2' values and the fat and water amplitudes may be erroneous. When the tissue contains only fatty components, the CH and CH_2 components, for example, may dominate and, because their chemical shift separation of 4 ppm is similar to that of water and CH_2 , the decomposition may cause errors associated with incorrect peak assignments and location. In this case, one could alter the τ values to correspond to the appropriate chemical shift and treat the fat signal as a simple two-component system.

Both techniques described here use τ values chosen to increment the chemical shift phase encoding by multiples of π . This is not strictly necessary, however. Other three-point schemes have been investigated, including $(-\pi/2, 0, \pi/2)$, $(0, \pi/2, \pi)$, $(-\pi/2, 0, 3\pi/2)$, and so forth. However, all these methods use out-of-phase images to compute the B_0 map, and thus they

have the same problems that plagued the original $(-\pi, 0, \pi)$ method. In addition, the S/N performance will not be as good as that of the techniques that use phase increments spaced uniformly around the 2π circle. For example, with phase increments of $(-\pi/2, 0, 3\pi/2)$, it can be shown for no amplitude loss that $NSA^* = 4/3$, which is only half that of the chosen method.

The choice of θ thus involves a trade-off between conflicting requirements. S/N performance is maximized when the chemical shift phase encoding is uniformly spaced through 2π . However, this guarantees that there will be out-of-phase images in the B_0 calculation, and thus cancellation artifacts can occur. In addition, the analysis is difficult for arbitrary θ when amplitude losses due to dephasing are included. Thus, the best choice for the 3PD method seems to be θ equal to π , despite the slight reduction in NSA^* .

These multipoint Dixon methods should be thought of as a means of characterizing one or two additional parameters for an essentially two-component system by means of modeling, not for accruing substantial additional chemical shift resolution. It is in this regard that the 4PD method provides one additional parameter for the fat component over that of the 3PD method, which apparently produces more accurate T_2' assessment in subcutaneous fat (and presumably bone marrow as well).

The present method forces retention of two components in the chemical shift spectrum. Alternatively, one could model the fat component by the addition of a second line to the fat spectrum (CH or CH_3 , as appropriate for the tissue) and use the fourth measurement in the 4PD method for assignment of the three amplitudes, a common T_2' loss, and B_0 . This philosophy begins to approach that of classical spectroscopy. In the limit of desiring to characterize many additional parameters, one may be better off gathering a full chemical shift spectrum rather than attempting to model it a priori. ●

Acknowledgments: The author is particularly grateful to Jill Fredrickson, MS, and Ann Shimakawa, MS, for pulse sequence development, to Chris Wilbricht, MS, for a Signa 4.0 release reconstruction program, and to Erika Schneider, PhD, for useful discussions as well as comments on the manuscript. He is indebted to Denis Le Bihan, MD, PhD, for providing unpublished data on self-diffusion in lipids.

References

1. Dixon WT. Simple proton spectroscopic imaging. *Radiology* 1984; 153:189-194.
2. Buxton RB, Wismer GL, Brady TJ, Rosen BR. Quantitative proton chemical shift imaging. *Magn Reson Med* 1986; 3:881-900.
3. Szumowski J, Plewes DB. Fat suppression in the time domain in fast MR imaging. *Magn Reson Med* 1988; 8:345-354.
4. Yeung HN, Kormos DW. Separation of true fat and water images by correcting for magnetic field inhomogeneity in situ. *Radiology* 1986; 159:783-786.
5. Schneider E, Glover GH. Rapid in-vivo proton shimming. *Magn Reson Med* 1991; 18:335-347.
6. Lodes CC, Felmler JP, Ehman RL, et al. Proton chemical shift imaging using double and triple phase contrast acquisition methods. *J Comput Assist Tomogr* 1989; 13:855-861.

7. Tamler B, Sommer FG, Glover GH, Schneider E. Prostatic MR imaging performed with the three-point Dixon technique. *Radiology* 1991; 179:43–47.
8. Keller PJ, Hunter WW, Schmalbrock P. Multisection fat-water imaging with chemical shift selective presaturation. *Radiology* 1987; 164:539–541.
9. Haase A, Frahm J. Multiple chemical-shift-selective NMR imaging using stimulated echoes. *J Magn Reson* 1984; 64:94–102.
10. Petroff OAC. Mini-review: biological ^1H NMR spectroscopy. *Comp Biochem Physiol* 1988; 90B:249–260.
11. Vold RL, Vold RR, Simon HE. Measurements of transverse relaxation time in homonuclear coupled spin systems. *J Magn Reson* 1974; 13:226–231.
12. Wehrli FW, Ford JC, Kaut-Wilson C. Quantitative MR: a new method for in vivo characterization of trabecular bone structure. *Radiology* 1990; 177(P):245.
13. Ford JC, Wehrli FW. In vivo quantitative characterization of trabecular bone by NMR interferometry and localized proton spectroscopy. *Magn Reson Med* 1991; 17:543–551.
14. Bergin CJ, Glover GH, Pauly J. Lung parenchyma: Magnetic susceptibility in MR imaging. *Radiology* 1991; 180:845–848.
15. Majumdar S, Thomasson D, Shimakawa A. Magnetic field inhomogeneity effects induced by the susceptibility differences between trabecular bone and bone marrow in gradient echo magnetic resonance imaging: experimental studies. *Magn Reson Med* (in press).
16. Mayo JR, McKay A, Mueller NL. T2 relaxation time in MR imaging of normal and abnormal lung parenchyma. *Radiology* 1990; 177(P):313.
17. Glover GH, Schneider E. Three-point Dixon technique for true water/fat decomposition with B_0 inhomogeneity correction. *Magn Reson Med* 1991; 18:335–347.
18. Sepponen RE, Sipponen JT, Tantt JI. A method for chemical shift imaging: demonstration of bone marrow involvement with proton chemical shift imaging. *J Comput Assist Tomogr* 1984; 8:585–587.
19. Hahn EL. Spin echoes. *Phys Rev* 1950; 80:580–594.
20. Carr HY, Purcell EM. Effects of diffusion on free precession in nuclear magnetic resonance experiments. *Phys Rev* 1954; 94:630–638.